An Economical Tunable-Diode Laser Spectrometer for Fast-Response Measurements of Water Vapor in the Atmospheric Boundary Layer

Emily D. Wein[1], Lars E. Kalnajs[2], Darin W. Toohey[1]

[1]Department of Atmospheric and Oceanic Sciences, University of Colorado Boulder, Boulder, Colorado, USA

[2]Laboratory for Atmospheric and Space Physics, University of Colorado Boulder, Boulder, Colorado, USA

Correspondence to: Emily Wein (Emily.wein@colorado.edu) and Darin Toohey (Toohey@colorado.edu)

Abstract.

Water vapor in the atmospheric boundary layer poses a significant measurement challenge with abundances varying by an order of magnitude over short spatial and temporal scales. Herein, we describe the design and characterization of an economical and flexible fast-response instrument for measurements of water vapor. The in situ method of tunable diode laser absorption spectroscopy in the short-wave infrared was chosen based on a heritage with previous instruments developed in our laboratory and flown on research aircraft. The instrument is constructed from readily available components and based on low-cost distributed feedback (DFB) laser diodes that enjoy widespread use for high-speed fiber-optic telecommunications. A pair of versatile, high-speed Advanced RISC Machine (ARM) based microcontrollers drive the laser and acquire and store data. High precision and reproducibility are obtained by tight temperature regulation of the laser with a miniature commercial proportional-integral (PI) controller. The instrument is powered by two rechargeable 3.6 V lithium-ion batteries, consumes 2 W of power, weighs under 1 kg, and is constructed from hardware costing less than $3,000. The new Tunable Diode Laser Spectrometer (TDLS) agreed to within 2% compared to a laboratory standard and displayed a precision of 10 ppm at a sample rate of 10 Hz. The new instrument is robust and simple to use and will allow users with little previous experience in laser spectroscopy to acquire high-quality, fast-response observations of water vapor for a variety of applications. These include frequent horizontal and vertical profiling by uncrewed aerial vehicles (UAVs), long-term eddy covariance measurements from fixed and portable flux towers, and routine measurements of humidity from weather stations in remote locations such as the polar ice caps, mountains, and glaciers.

1 Introduction

The sources, sinks, and transport of water vapor within the atmospheric boundary layer (ABL) are key components of radiation budgets and meteorology (Trenberth et al., 2005). Water vapor mixing ratios in the ABL display high spatiotemporal variability due to the complex nature of land-surface interactions that drive sources and the clouds/precipitation that drive sinks (Santanello et al., 2018). At large scales, mixing ratios vary from 1500 parts per million by volume (ppmv) in the Arctic to

Deleted: The high spatiotemporal variability of water
Deleted: possesses
Deleted:
Deleted: in the atmospheric boundary layer (ABL).
Deleted: -
Deleted: -
Deleted: (TDLS)
Deleted: (SWIR)
Deleted: (DFB)
Deleted: ARM-
Deleted: via
Deleted: integrating
Deleted: can be
Deleted: 5
Deleted: comprised of
Deleted: agrees
Deleted: displays
Deleted: allows
Deleted: instrumentation
Deleted:
Deleted: to
Deleted: displays
Deleted: (Santanello et al., 2018) and clouds and precipitation that drive sinks (Larson et al., 2002). At large scales, boundary layer water vapor mixing ratios vary from 1500 parts per million (ppm) in the Arctic to 25,000 ppm in the Tropics, and

25,000 ppmv in the tropics, whereas they can range over five orders of magnitude from the surface to the upper troposphere (Wulfmeyer et al., 2015). On scales of 100 to 1000 m, mixing ratios vary by tens of percent because of differences in local land surface, temperature dynamics, and wind fields (Fischer et al., 2012; Kiemle et al., 2011; Shivers et al., 2019). Observations of this variability are essential for elucidating the underlying micrometeorological processes and quantifying local-scale (100 m) radiation budgets important to the prediction of turbulent and convective processes and their impacts (Couvreux et al., 2009; Fabry, 2006; Ogunjemiyo et al., 2002). However, observations have been limited by the relatively high cost of existing instruments and the lack of high-quality data from more economical ones (Geerts et al., 2018).

Satellite-based remote sensing measurements are too coarse to resolve important variations of water vapor on very small scales (Trent et al., 2018). Therefore, fast-response in situ and LIDAR-based instruments have become the primary methods for observing water vapor from the surface and mobile platforms for process-oriented studies. The latter (e.g., differential absorption LIDARS and Raman LIDARs), capable of multidimensional measurements with spatiotemporal resolutions of 10 m to 100 m and greater than 1 s, are deployed frequently for profiling the ABL (Wulfmeyer et al., 2015). However, relatively high cost and operational demands limit their usefulness for more widespread deployment. Alternatively, fast response in situ instruments have found increasing use in a variety of applications for measurements of small-scale variations in the ABL. They capture the smallest and fastest atmospheric variations near the surface where the atmosphere is not well mixed (Geerts et al., 2018). Incorporating high sampling rates faster than 1 Hz, instruments such as infrared gas analyzers (IRGAs) that rely on non-dispersive infrared light are typically used to monitor surface-based fluxes of H_2O and CO_2 within ecosystems (Aubinet et al., 2012). These research-grade instruments, which are used predominantly at multi-instrumented flux towers and weather stations, tend to be expensive, often costing $20,000 or more. In addition, they can incur additional costs for factory service to maintain high accuracy. Consequently, their use in remote locations has been relatively limited.

At the other end of the cost spectrum are various versions of capacitive humidity sensors that have found frequent use among hobbyists and research scientists for routine measurements from surface weather stations (Muller et al., 2015). These tiny sensors, costing only tens to hundreds of dollars, employ thin-film water-sensitive polymers sandwiched between two electrodes. They have been used in radiosondes for more than 40 years, and they can be accurate to ~0.8 % over a wide range of humidities. Although they are small and relatively inexpensive, they respond slowly to changes in water vapor, and they exhibit measurement biases that limit their usefulness for high-frequency observations (e.g. Miloshevich et al., 2009, 2004; Segales et al., 2022).

As fast in situ observations of H_2O are essential for numerical weather prediction and for investigations of the evolution of the ABL and its turbulence characteristics (e.g. large eddy simulations), and there is a need for more frequent measurements from remote locations, we have developed an economical new fast-response laser spectrometer (Helbig et al., 2021; Petersen, 2016). The instrument is capable of fast measurements of water vapor in the ABL, while demonstrating high accuracy and precision comparable to that of commercially available research-grade commercial instruments. Built from low-cost components that are readily available commercially, the instrument exhibits relatively low up-front costs with the ability to

Deleted: water vapor can

Deleted: precent

Deleted: mesoscale meteorological processes and quantifying local-scale (100 m) radiation budgets (Fabry, 2006; Ogunjemiyo et al., 2002). Observations of the ABL and its variability with high spatial and temporal resolution are necessary to resolve outstanding issues related to the prediction of turbulent and convective processes and their impacts. However, observations have been limited by the relatively high cost of existing instruments and lack of high

Deleted: , therefore

Deleted: DIALS

Deleted: Lidars

Deleted: , are deployed frequently for profiling the ABL; however, their

Deleted: -

Deleted: capturing

Deleted: the

Deleted: have come

Deleted: routinely

Deleted: To date these instruments, tend to be highly specialized and available from a small number of vendors as research-grade tools for observations from weather stations or flux towers. In addition, they typically cost $20,000 or more and they require frequent maintenance and calibration from the original factory.

replace critical components, thus bridging the gap between the more expensive and highly accurate fast-response instruments and the relatively inexpensive, but slower response capacitive sensors.

The design described here is an adaptation of previous instruments that have a 30-year history of use on research aircraft including the NASA ER-2, DC-8, WB-57F, and NCAR GV (Davis et al., 2007; Dorsi et al., 2014; Hallar et al., 2004; May, 1998; May and Webster, 1993; Newell et al., 1996). As in those instruments, it employs a commercial telecommunications fiber-coupled distributed feedback (DFB) laser in a common butterfly package with self-contained thermoelectric coolers (TEC) for precise selection of wavelength and for reducing absorption by water vapor in trapped spaces in complex coupling optics (Dorsi et al., 2014). The instrument is built from commercial off-the-shelf components, and it exhibits performance comparable to instruments costing an order of magnitude more. The new design is flexible and simple, allowing for accurate and reliable measurements of water vapor for investigators with little previous experience in laser spectroscopy while being easily adaptable to different contexts and other atmospheric species.

Several immediate applications are envisioned for this new instrument. One involves fast-response, open-path observations of water vapor from a small uncrewed aerial vehicle (UAV) such as a hexacopter. While this application has already been explored such as in Bärfuss et al. (2023); Pillar-Little et al. (2021); Segales et al. (2020); Varentsov et al. (2023) the instruments used have slow response times, resulting in limited vertical resolution (Segales et al., 2022). The instrument described in this paper would be ideal for obtaining observations over very small scales (e.g., centimeters), including obtaining frequent high-resolution thermodynamic profiles at locations such as remote land and ocean regions where observational gaps limit numerical weather prediction and climate modeling (Brotzge et al., 2023; Kämpfer, 2013). Another application is tracking water-resource loss from reservoirs with ground-based flux measurements. There is a need to increase the density of measurements on specific reservoirs to map out the heterogeneous scalar and vector fields resulting from complex terrain (Friedrich et al., 2018). Expanding sensor networks with economical instruments that maintain high accuracy and precision to monitor evaporation in regions of complex terrain can open up new areas of study and fill gaps where there is limited knowledge of the importance of evaporation to water availability, especially in arid regions (Roth and Blanken, 2023). Such a capability will also enable new studies of ecosystem exchange in geographic regions that have been historically underserved, for example in developing countries (Kim et al., 2022; Markwitz and Siebicke, 2019).

2 Instrument Design

2.1 Hardware Description

The TDLS instrument described here is based on a design reported previously for measurements of condensed water contents from research aircraft (Dorsi et al., 2014). A DFB laser diode (NLK1E56AA, NTT Innovative Devices, Yokohama, Japan) emitting radiation with a wavelength centered at 1368.6 nm at room temperature rapidly scans over a strong water vapor absorption line. To avoid damping of high-frequency variations, a short (~20 cm), open-path, single-pass optical cell was constructed of low-cost commercial components. Water vapor mixing ratios in the range 2000-20,000 ppm are readily retrieved

Deleted: ¶
As fast in situ observations of H_2O are essential for numerical weather prediction and for investigations of the evolution of the ABL and its turbulence characteristics (e.g. large eddy simulations) (Helbig et al., 2021; Petersen, 2016), a more economical instrument capable of fast, high-accuracy measurements of water vapor in the ABL is desirable. Here, we report on the development and performance of a new TDLS capable of fast-response measurements of water vapor in the ABL. Demonstrating high accuracy and precision matching that of commercially available research-grade commercial instruments, yet exhibiting lower cost and greater flexibility, the instrument bridges the gap between the more expensive and highly accurate fast-response instruments with the relatively inexpensive, but slower response capacitive instruments.

Deleted: technology

Deleted: (e.g.

Deleted: .,

Deleted: ;

Deleted: .,

Deleted: ;

Deleted: .,

Deleted: ;

Deleted: .,

Deleted:)

Deleted: available instrumentation

Deleted: and

Deleted:

Deleted: modelling

Deleted: effect of terrain and variable field inhomogeneity

Deleted: an

Deleted: instrument

Deleted: maintains

Deleted: where there is a need for simultaneous observations

Deleted: (Markwitz and Siebicke, 2019; Kim et al., 2022)

Deleted: off

Deleted: ; a schematic of which is shown in Fig. 1.

Deleted: (NLK1E56AA, NTT Innovative Devices, Yokohama, Japan)…

with high precision (+/- 10 ppm). The primary novelty of the new TDLS is a low-power, low-cost electronics package that simultaneously drives the laser with rapid linear current ramps over a highly stable wavelength range while acquiring data for subsequent processing of the scans into accurate mixing ratios based on laboratory calibrations. An overview of the instrument is depicted in Fig. 1.

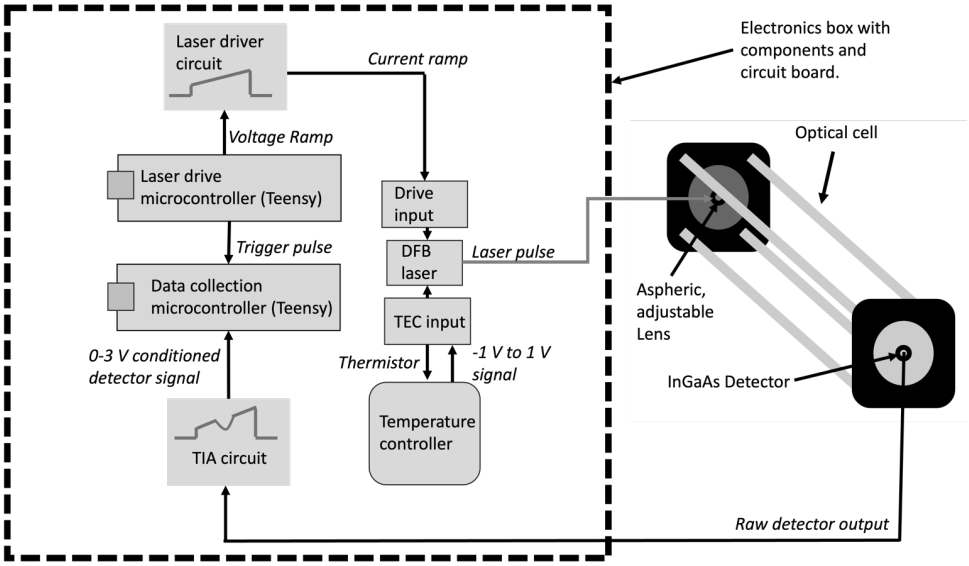

Figure 1. Schematic diagram of the new TDLS. Arrows represent the direction of information flow between individual components (microcontrollers, laser, temperature controller) or individual circuits (transimpedance amplifier, or TIA, and laser driver). The dotted line indicates all components contained on the printed circuit board and those housed outside. A fiber optic coupler and twisted wire pair are passed outside the electronics box through hermetically sealed holes.

The laser is tuned to the wavelength of a strong water absorption feature centered at 1368.59 nm by changing the temperature of the laser diode with a commercial PI TEC controller (WTC 3243, Wavelength Electronics, Bozeman, MT) (Gordon et al., 2022). Temperature is maintained at ± 0.002 K of the setpoint, consistent with the manufacturer's specification. The setpoint is derived from a voltage divider sourced with a high-precision reference (e.g., LDLN025M25R, STMicroelectronics, Geneva, Switzerland) and a variable resistor. This stability is important for maintaining a reproducible

Deleted: .¶ ¶ The

Deleted: proportional-integral (

Deleted:)

Deleted:).

Deleted: A highly stable temperature of

Deleted: , is maintained with a fixed set point

output wavelength of the laser. If desired, a voltage from a digital-to-analog (DAC) output can be used for dynamic temperature control.

Two Teensy Arduino-compatible microcontrollers were chosen for the laser driving ("driver") and data acquisition ("receiver") functions. These microcontrollers are based on low-cost ARM Cortex-M processors, exhibiting a balance of speed and flexibility. Previous instruments developed in our lab and elsewhere that employ the same measurement technique as reported here use single or multi-core general-purpose processors running full operating systems such as Linux on a PC-104 form factor single board computer (e.g. Hallar et al., 2004; Dorsi et al., 2014). Unpublished work in our lab showed that imprecise timing of the output ramp for the laser caused by software interrupts produced an unstable PI temperature of the DFB TEC that resulted in wavelength "jitter" (movement of the position of the line center in the laser scan) (Rainwater, 2022). Separating the input and output functions allows for precise control of the laser and highly reproducible scans up to ~1 kHz resulting in high-resolution measurements. The microcontrollers simplify the electronics while also allowing for uninterrupted laser scanning while the detector signal is acquired, processed, and stored.

A Teensy 3.6 with integrated 12-bit, 10^5 samples per second DAC provides the drive voltage for scanning the laser current. The middle panel in Fig. 2 shows an example of a series of linear ramps used as the drive function of this instrument, each consisting of 1366 discreet one-bit steps from 0.80 V to 1.9 V. This voltage drives an operational amplifier (Analog Devices LT1101) that controls the current required to scan the laser from a transistor (TIP 32AG n-channel Transistor) in a textbook voltage-to-current converter circuit (Figure 6.31 of Horowitz and Hill, 1983). A complete electronics circuit diagram of the instrument is shown in Fig. 3. The scan rate, current range, and a pause for background time are configured in software. Before the start of each scan, the Teensy 3.6 produces a digital pulse ("trigger"), shown on the bottom panel of Fig. 2, that initiates the data acquisition and storage process on a Teensy 4.1. At this time, the internal clock is recorded into a buffer, and the output from the detector TIA is recorded as a single scan consisting of 445 discreet samples at 12-bit resolution. Although the Teensy 4.1 samples at 300 ksps, we oversampled 32 times using a software function that reduces noise inherent in the analog-to-digital converter (ADC). This resulted in a minimum resolvable signal of ~0.2 mV.

Deleted: DFB
Deleted: the
Deleted: from one of the microcontrollers
Deleted: also
Deleted:
Deleted: are
Deleted: -
Deleted: -
Deleted:)
Deleted: off
Deleted: RISC
Deleted: configurability.
Deleted: employed
Deleted:
Deleted: Hallar et al., 2004; Dorsi et al., 2014).
Deleted: (Rainwater, 2022)
Deleted: result
Deleted:).
Deleted: 10
Deleted: and faster
Deleted: precision of the
Deleted: 10^6
Moved (insertion) [1]
Deleted: DFB current. Prior to
Deleted: was used for data acquisition and storage with a built in Micro-SD card feature. Upon receiving the trigger pulse
Deleted: ADC is started. The top panel in Fig. 3 shows
Deleted: acquired
Deleted: output
Deleted: points (7.2 kHz raw ADC rate) sampled
Deleted: ,
Deleted: built-in averaging
Deleted: to reduce
Moved up [1]: The middle panel in Fig.
Deleted: Teensy. This results
Deleted: 3 shows an example of a series of linear ramps, each consisting of 1366 discreet one-bit steps from 0.80 V to 1.9 V.

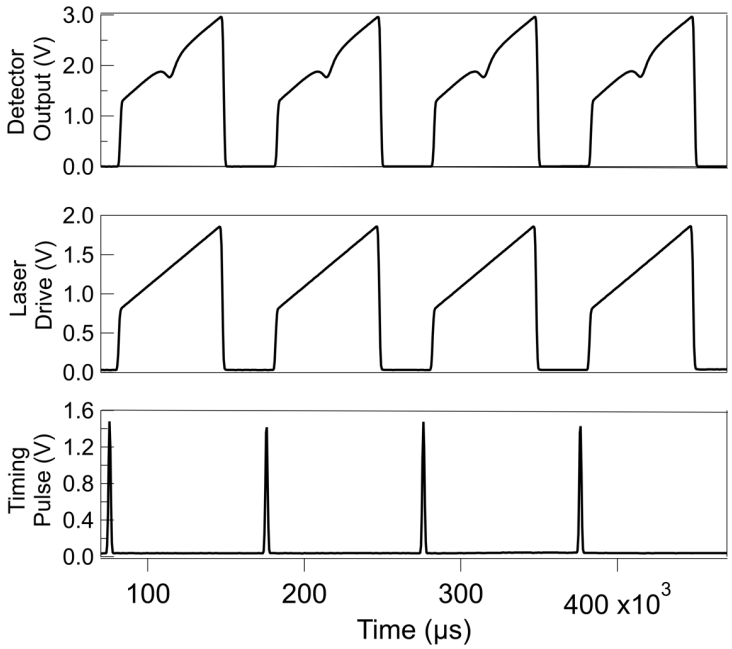

Figure 2. Important components of the TDLS laser scans as a function of time. The detector output (top panel) is the continuous voltage from the TIA. About one-third of the time the laser is off, and the signal is close to zero. This is the background for the detector and TIA circuit. The laser drive (middle panel) represents the voltage output by the Teensy 3.6 used to set the current of the laser. The trigger pulse signal (bottom panel) is sent by the Teensy 3.6 to the Teensy 4.1 to initiate the sampling and recording of the scan.

For this work, a single pass, open-path, 21.5 cm optical cell was constructed with a fixed 30-mm cage plate assembly (Thorlabs, Newton, NJ). One end housed an adjustable aspheric collimating lens (CFC11A-C Adjustable Fiber Collimator, FC/APC, f = 11.0 mm, 1050 - 1620 nm AR, Thorlabs, Newton, NJ) that was attached to the FC/APC output of the laser. The lens was configured so that the laser beam was divergent to fully illuminate the active area of a low-noise broadband indium gallium arsenide (InGaAs) semiconductor photodiode and reduce variations in intensity due to vibration and turbulent fluctuations of air density in the optical path. Multiple photodiodes of differing manufacturers (Thorlabs FDGA05, ThorLabs FGA04, Fermionics FD1500) were used throughout this work, with no significant difference in results or performance. The photodiode was operated in photovoltaic mode, and the photocurrent was converted to a voltage up to a maximum of 3.3 V

Deleted: Detector signal (top panel),

Deleted: voltage

Deleted:), and

Deleted:). See text for explanation.

Deleted: DFB

Deleted: ,

Deleted: divergence of which

Deleted: opened

Deleted: (either Thorlabs FDGA05 or Fermionics FD1500) on the opposite side of optical path both operated in photovoltaic mode. Intensity

Deleted: are minimized as the beam width is larger than the active area of the photodiode.

Deleted: is

Deleted: is

with a custom-built low-noise transimpedance amplifier circuit using a single-supply operational amplifier amp (LT1013 CN8, Analog Devices, Wilmington, MA). The top panel in Fig. 2 shows the continuous output of this circuit. The gain was tuned using a 1-10 kΩ variable resistor.

The two Teensy microcontrollers, laser temperature controller, detector amplifier, batteries, and power conditioning were placed on a custom-built circuit board (OSHPark, Portland, OR). The instrument was powered on or off with a single-pole-single-throw toggle switch, with a small light-emitting diode (LED) that indicates when the instrument is running. An LED on the Teensy 4.1 indicated when data were being written to the MicroSD card. The instrument consumes 2.0 W of power, and it can operate for 2 h when powered by two 3.6 V rechargeable lithium-ion batteries (e.g., ARB-L16-700UP, Fenix Lighting, Littleton, CO). Alternatively, it can be run indefinitely from a DC power supply, including 5 V passed through either of the Teensy microUSB inputs. All components, except the optical cell, coupling laser fiber-optic cable, and twisted-pair of electrical wires leading to the detector, were packaged in a box with dimensions of 16.18 x 11.18 x 4.90 cm (PN-1324-C, Solutions Direct, Riverside, CA).

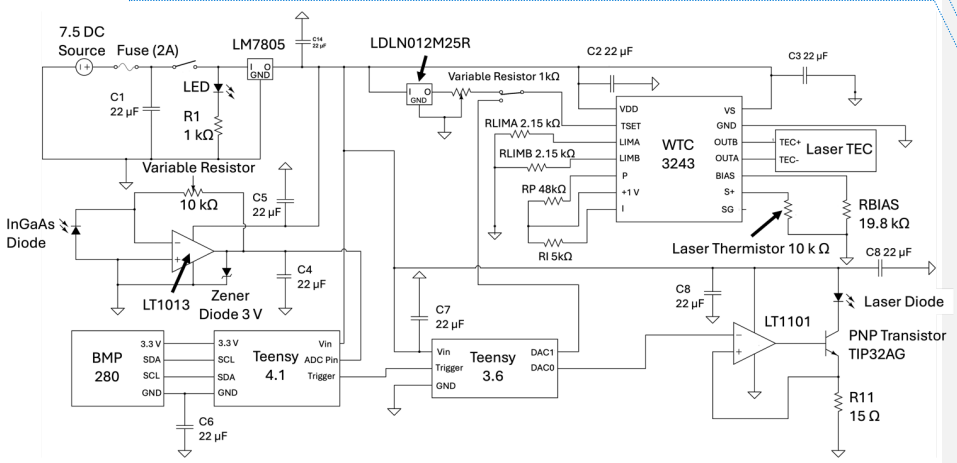

Figure 3. The circuit diagram of the instrument is shown here including all components and power conditioning. Specific components used in the design are labeled where applicable. Power is provided by two batteries (7.5 V total) and passed through the LM7805 chip to supply 5 V to the board. There are 5 major circuits or components included in the design: the WTC circuit, the laser drive circuit, the TIA amplifier, and the Teensy 3.6 and 4.1.

Deleted: AD1101
Deleted: could be
Deleted: a variable resistor, was adjustable with
Deleted: is
Deleted: receiver
Deleted: indicates
Deleted: are
Deleted: entire system
Deleted: 5
Deleted: the instrument
Deleted: via
Deleted: input
Deleted: and
Deleted: , can fit
Deleted:), with the laser output fiber and twisted pair of wires from the detector passing through a hermetic seal.

2.2 Spectral Processing

Water vapor concentrations are derived using the approach described previously (Dorsi et al., 2014). Fig. 4a shows a single scan over the absorption line consisting of 445 individual measurements of the amplified detector signal. Briefly, a small detector/amplifier offset is determined from 10 points each at the start and end of each scan while the laser is powered off. Then, linear segments near the beginning and end of the linear current ramp outside of the water vapor absorption feature are identified for calculating the background (i.e., $I_0(t)$) based on a linear fit (dashed line in Fig. 4a).

To account for possible drift of laser wavelength (e.g., the position of the absorption feature in a scan), a relationship between scan position and laser wavelength was estimated using a closely spaced pair of weak water absorption lines at 7281.72 and 7281.80 cm^{-1} produced by a DFB laser-centered on a different wavelength than the one used for the measurements in this paper. The position of this pair was systematically scanned across the full temperature range of a single current ramp by slowly varying the setpoint of the WTC and the spacing between the two lines (0.08 cm^{-1}, or 0.015 nm) was measured in scan index (e.g., see Fig. 4). A linear fit to the ratio of this spacing to the difference in scan index as a function of scan position was determined as:

$$s(x)\ (nm/step) = 0.00052 + x * 5.00 * 10^{-7}$$

where s is the change in wavelength per scan index (of the 445 points) and x is the scan index. The use of this function results in a near-constant line width as a function of wavelength if the position of the absorption feature shifts slightly due to variations in laser baseplate temperature. Although such a shift was never observed in these experiments, it is a consideration for use in an environment where the ambient temperature may vary significantly – e.g., by many tens of degrees. This method also allowed for the determination of the full width of the scan to be 0.279 nm for the specific scan start and end points and scan rate used in these experiments.

Based on the Beer-Lambert Law, water concentration is proportional to the integral of absorbance $A = ln(I_o/I)$ over the full width of the absorption line. This integral is estimated as the sum of discreet points as in Eq. (1).

$$\int A(\lambda)\, d\lambda = \sum_{k=1}^{385} A(\lambda)_k * \Delta\lambda_k \quad (1)$$

An example of a single laser scan converted to absorbance is shown in Fig. 4b. The resulting integral is related to concentration of water vapor by a response factor determined by laboratory calibration using a high-accuracy cavity ringdown spectrometer, CRDS (L-2120i, Picarro, Santa Clara, CA), referenced to a dew-point generator (LI-610, LiCor, Lincoln, NE) (Henze et al., 2023; Noone et al., 2011). Ambient water concentrations and mixing ratios are interchangeable through the ideal gas law using concurrent measurements of temperature and pressure, which, for this work, were measured with a small sensor (BMP280, Bosch Sensortec, Reutlingen, Germany) placed midway between the output lens of the laser and the detector just outside the

Deleted: Figure

Deleted: 30

Deleted: 20 from the

Deleted: 1st-order polynomial

Deleted: Scan step number (or elapsed time) is converted to

Deleted: based on an empirical function derived by

Deleted: the spacing of line centers of a

Deleted: as a ruler when mapping the laser tune range as a

Deleted: of laser TEC temperature. This is convenient

Deleted: it accounts for the possible drift of the tune

Deleted: by removing the nonlinear output laser wavelength in response to a linear current ramp and

Deleted: us to determine

Deleted: . The observed signal (i.e., $I_{obs}(t)$) and calculated background $I_0(t)$ are then placed in an array $[\lambda_o, I_o(\lambda_i), I(\lambda_i)]$.

Deleted: (Noone et al., 2011; Henze et al., 2023). Ambient water concentrations and mixing ratios are interchangeable through the Ideal Gas Law using concurrent measurements of temperature and pressure, which, for this work, were measured with a small sensor (BMP280, Bosch Sensortec, Reutlingen, Germany) placed midway between the output lens of the laser and the detector just outside the laser beam. The precision of this sensor was measured to be +/-1 Pa and +/-0.01° C

laser beam. The precision of this sensor was measured to be +/-1 Pa and +/-0.01° C with an accuracy of ± 1 % when compared to laboratory standards.

For this work, we store the raw scan data with T, P, and a timestamp and perform data analysis in post-processing using code written in Python. This maximizes precision and flexibility while allowing us to evaluate performance with various diagnostic variables (e.g. those investigating stability or interference) that are readily derivable from raw scans. Future iterations of this design will be simplified to include real-time processing of the spectra on the Teensy 4.1 before data are written on the microSD card. Processing of spectra in real time takes a fraction of the clock cycles needed for writing an entire raw scan and will not affect instrument time response. The Arduino sketches and processing codes are available on GitHub.

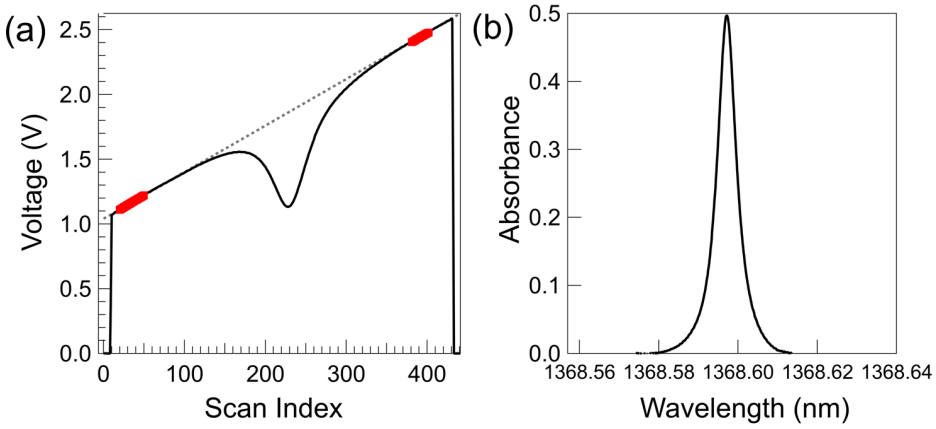

Figure 4. (a) Example of the output of the TIA for a single scan of the DFB laser consisting of 445 discreet points. The dashed line is a linear fit in a region where absorbance by H_2O is negligible (defined as I_0). The fit is made between the points highlighted in red (30 points at the start of the scan and 20 at the end). (b) Absorbance is defined as $\ln(I_0/I)$ for a single scan of the DFB laser. The integral signal is calculated by integrating over the calculated absorbance by integrating with respect to wavelength.

3 Results

The TDLS integrals were calibrated by sampling a range of mixing ratios from 5,000 ppm to 25,000 ppm reported by the CRDS in an unsealed 250 L Polycarbonate chamber alongside the CRDS. The TDLS optical cell was placed in the center of the chamber, and a fan was used to ensure the chamber was well-mixed. The sampling line of the CRDS was aligned with

Deleted:
Deleted: only
Deleted:
Deleted: These calculations take
Deleted: so don't
Deleted: In the meantime, we have uploaded our
Deleted: to
Deleted: opensource
Deleted: transimpedance amplifier
Deleted: . The initial ~10 points and final ~10 points represent the signal with the laser powered off
Deleted: shown in Fig. 3. Wavelength is determined as described in the text.
Deleted: series
Deleted: spanning the range
Deleted: 27
Deleted: a
Deleted: -
Deleted: assure
Deleted:

the mid-point of the TDLS open-path cell and positioned just outside the path of the laser beam. A beaker of warm water was placed inside the chamber to humidify the air to a value below the saturation point at lab temperature. Over two hours, mixing ratios were reduced to ~13,000 ppm by stepwise addition of relatively dry ambient air from the laboratory into the chamber. Thus, a series of values spanning the range 13,000 ppm to 25,000 ppm was obtained. Values below 13,000 ppm were produced by further dilutions using a flow of dry air from a cylinder of Ultra Zero Air (H_2O < 2 ppm, total hydrocarbons < 0.1 ppm, Airgas, Dacono, CO). TDLS concentrations were converted to mixing ratios using pressure and temperature as measured from the BMP280 sensor, and the results are shown in Fig. 5. The deviation between the two data sets is less than 2 % over the range of 5000 ppm to 25,000 ppm. This is larger than the precision of the Picarro, which is ~10 ppm, and so the deviation is mostly due to small differences in water vapor in the paths sampled by the two instruments.

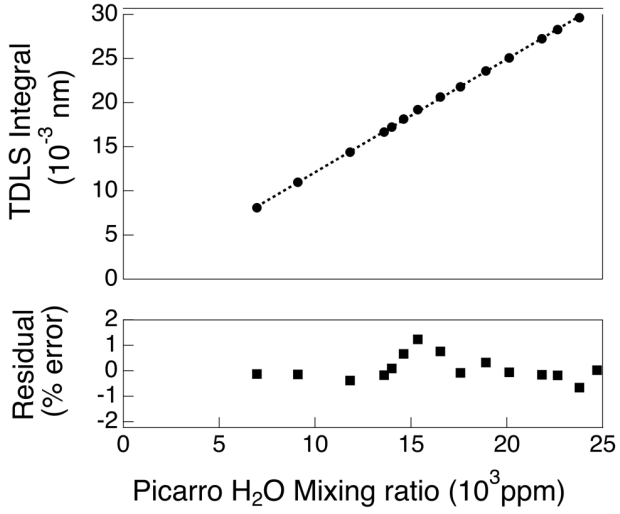

Figure 5. Top: Integral signal of the TDLS calculated as described in the text as a function of water vapor mixing ratio (black points) determined by simultaneous measurements with a Picarro L-2120i cavity ringdown spectrometer. The dashed line represents a linear fit to the results over the range 7,000 – 25,000 ppm. Bottom: Residual error, as percent of measurement, plotted for each of the points in the top panel. Fit Parameters: slope = 0.0006, intercept = 0.0039, R^2 = 0.9999.

Deleted: The
Deleted: was first saturated
Deleted: mixing ratio of ~27,000 ppm with the dew
Deleted: generator, after which lab air with
Deleted: H_2O was admitted to
Deleted: stepwise approximately every five minutes over the course of several hours.
Deleted: 27
Deleted: lower than
Deleted: 5000 ppm to 25,000 ppm
Deleted:).
Deleted: (e.g., Noone, et. al, 2008).
Deleted: 29

The precision and stability of the TDLS under controlled laboratory conditions were assessed using a standard Allan variance analysis (Werle et al., 1993). Precision is taken to be the square root of the Allan-Variance at the highest sample rate. To reduce variations in ambient water vapor, the output fiber of the laser was attached to one end of the 53.3-cm long sample cell of the CU second-generation closed-path laser hygrometer (CLH-2) that was held at fixed pressure and temperature. The signal was detected with an InGaAs FC/APC-coupled detector (ThorLabs FGA04) as described elsewhere (Dorsi, et al., 2014). In this manner, electronic noise and drift could be assessed independently of variations in pressure, temperature, and water concentration. An Allan-variance analysis of results, shown in Fig. 6, demonstrates a precision of 10 ppm at 0.1-s response time for a water abundance of 11,800 ppm. This represents a fractional absorbance of 10^{-3} for the conditions of the test. Averaging (increased integration time) allows the precision to be improved by an order of magnitude down to 0.9 ppm at 34 s corresponding to a sensitivity of 1 in 10^{-4}.

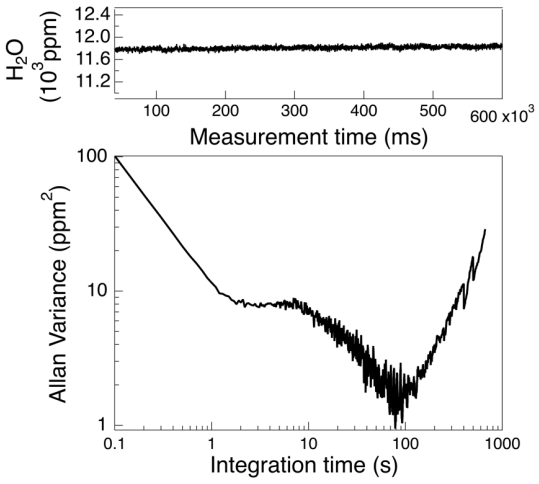

Figure 6. Top: Time series of water vapor mixing ratio for a 10-min segment from a laboratory measurement in a sealed absorption cell held at constant temperature and pressure. Bottom: Allan variance calculated from the segment of data displayed in the top panel. The instrument demonstrates a precision of 10 ppm at 10 Hz (the intercept in the bottom panel).

The performance of the TDLS was assessed in several "real world" demonstrations. The goals of which were to demonstrate stability for long-term observations and accurate quantification of fast variations of water vapor. The first demonstration was an intercomparison with a commercial analyzer with a long history of eddy covariance measurements of CO_2 and H_2O in a variety of environments (e.g. Burns et al., 2009; Ocheltree & Loescher, 2007; Pokorný et al., 2012; Zhao &

Deleted: -Variance

Deleted: a

Deleted: This detector is distinct from the ones previously described in this paper and it was used only for this experiment to couple the instrument to the sample cell.

Deleted: independent

Deleted: sensitivity

Deleted: , the

Tans, 2006). The LI-7000 (LiCor, Lincoln, NE) is a high-performance, dual-cell nondispersive infrared (NDIR) instrument with an accuracy for H_2O of +/- 1% and a precision (RMS noise) of 2 ppm at 5 Hz (LI-7000 CO_2 /H_2O instruction manual; Publication 984-07364, 2007). The site chosen for this test was the exterior of our laboratory where large variations in H_2O would be expected from local sources such as vegetation and passing pedestrians. Fig. 7 shows the power series densities (PSD) for both instruments for a 1000-s segment of data.

At frequencies up to ~2 Hz, the two instruments exhibit similar behavior, with power dropping with increasing frequency following a –2/3 power law typical for long-lived atmospheric variations (Wu et al., 2015). Above 2 Hz, the Li-7000 power spectrum deviates below this power law due to the damping of higher frequencies characteristic of closed-path measurements (Aslan et al., 2021). Conversely, the power spectrum of the TDLS trends above the power law at > 3 Hz, exhibiting a measurement precision of ~10^{-3} absorbance, consistent with that determined from the Allan-variance analysis in the static cell, shown in Fig. 6.

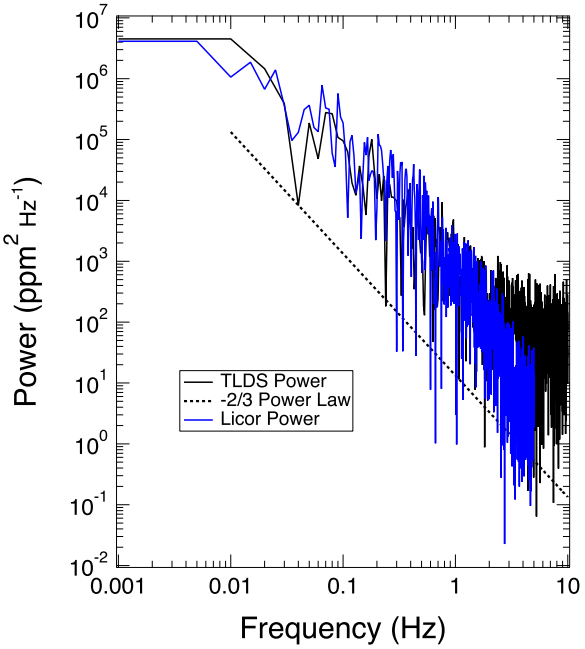

Deleted: of

Deleted:

Deleted:

Deleted: e.g., see

Figure 7: Power spectral density (PSD) of the Li-7000 and new TDLS as a function of measurement frequency. The dotted line is the -2/3 power law that is expected for variability of ambient H_2O. The Li-7000 PSD does not extend beyond 5 Hz, the maximum sample rate of the instrument.

To test the long-term stability of the TDLS (days), we performed a three-day intercomparison with the same L2120-i CRDS used for the calibrations described above. Both instruments were sampled from the top of a shipping container used for housing electronics in the Department of Atmospheric and Oceanic Sciences (ATOC) Skywatch Observatory located on East Campus (Lat 40.01° N 105.24° W, Elevation: 1600 m) on the University of Colorado Boulder. The CRDS and associated vacuum pump were placed inside the container, sampling from a 3-m long, ¼-in O.D. copper line running vertically up the side of the container and terminating with a 3.8-cm radius, 180° bend to avoid ingesting precipitation. The optical cell for the TDLS was installed at the same elevation approximately ~1.5 m from this inlet. A 25 m fiber optic patch cable connected the output of the laser to the collimating lens on the input of the optical cell and a 10 m twisted pair of wires brought the detector signal back to the TDLS electronics box which was housed in the shipping container. It is important to note that a better design would have placed the detector amplifier close to the detector to reduce noise pick-up; therefore, this setup likely represents the "worst case" noise of the TDLS for such a remote installation.

Observations from the TDLS and the CRDS instruments at their native resolutions of 10 Hz and 0.55 Hz, respectively, are shown for three continuous days in Fig 8a. Over this period, H_2O mixing ratios varied from 5,000 ppm to 12,000 ppm, and ambient temperature varied from 10.5 °C to 33.5 °C. There were multiple occurrences of precipitation and virga and periods of variable cloud cover and direct sunlight. There were several important outcomes from this test. First, the detector/amplifier zero signal from the TDLS (not shown here) varied from 0.006 V to 0.26 V (i.e., <10 % of average laser signal), from direct sunlight or reflections, thus providing a good test of the validity of the method described above for extracting water vapor mixing ratios from individual spectra. The background was successfully subtracted out before calculation, but this issue could be readily addressed in a proper field experiment by suitable baffling of the optics to block the incoming solar radiation. Second, the robustness and reliability of the spectroscopic foundation of the measurement were demonstrated by the successful acquisition of 4.17×10^6 unique and independent spectra over this period, with rejection of fewer than 0.05 % due to detector signal that was clipped or filtered when the scan background used to calculate I_o varied by more than 2 %. These losses of signal, which typically lasted only a few seconds and self-corrected, occurred during precipitation. They were likely due to condensed water blocking the light path.

A scatterplot of several days of continuous measurements by both instruments is shown in Fig. 8b. Over 5000 observations of 30-second averages are represented in this plot. The TDLS measurements were first averaged in bins of 20 measurements (e.g., to a 2-s time base) and the results were then merged with the matching times recorded by the CDRS. Both observations were then bin-averaged down to ~30 s to correspond with the digital smoothing inherent in the Picarro L-2120i instruments. The instruments show remarkable agreement over the entire sampling period, with a < 4% deviation from a 1:1 correspondence and a 0.993 coefficient of determination (R^2). It is noteworthy that this averaging has removed 80 % of the

Deleted: TLDS (e.g.,
Deleted: calibrating
Deleted: TDLS as
Deleted: The TDLS and CRDS
Deleted: Elev
Deleted: at
Deleted: sampled
Deleted: shipping
Deleted: TLDS
Deleted: A long electrical line and
Deleted: -
Deleted: long
Deleted: TDLS
Deleted: ,
Deleted: -
Deleted: long
Deleted: set-up
Deleted: sun
Deleted: was
Deleted: on May 4th
Deleted: the 3
Deleted: from the TDLS and CRDS
Deleted: to
Deleted: Despite being separated horizontally by ~1.5 m, the two

variability of ambient H_2O largely due to what is occurring on the fastest timescales including variability due to the Picardo inlet and optical cell being separated by 1.5 m.

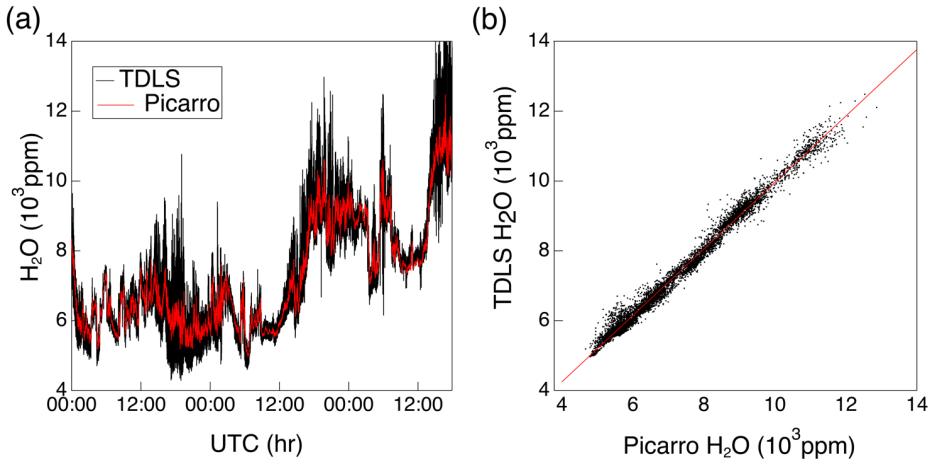

Figure 8: (a) Time series of Picarro and TDLS traces for a continuous sampling starting on May 5th at 00:00 and proceeding until around 17:45 on May 8th. (b) Scatterplot of 30-s averages of measurements from the TDLS (y-axis) and Picarro CRDS (x-axis).

The stability of the new TDLS was also assessed by examining three metrics of system performance, including detector signal at the start and end of each laser scan (representative of laser stability and optical efficiency), the ratio of these values (representative of laser and detector stability), and the position of the line center of the water vapor absorption feature (a direct measure of the temperature of the laser TEC). In all experiments described here, the ratio of amplified detector signal at the start and end of each scan was found to vary by less than 2 % after subtracting the zero-signal measured when the laser is powered off. In addition, the center position of the water vapor line drifted by +/- 1 scan index point or less from scan to scan. Based on a calibration of the temperature dependence of line position using the setpoint of the PI controller to vary laser TEC temperature, it was found that this stability corresponds to < 0.001 K, a result that is consistent with the specifications of the WTC-3243.

Deleted: from 5-8

Deleted: 2023. UTC time 300,000 corresponds to 11:19 local time on 5…

Deleted: Stability

4 Discussion

The goal of this work was to design, build, and characterize an economical and flexible fast-response instrument suitable for measurements of water vapor in the ABL. The entire electronics package is inexpensive and built with generalized components separated from the optical cell. A primary consideration was the use of low-cost, low-power, commercial off-the-shelf components that, when combined with readily available lasers used by the telecom industry, allow for high-quality, high-frequency observations at a fraction of the cost of commercial instruments with similar measurement characteristics. The key enabler for this new TDLS is the family of ARM-based microcontrollers based on the Cortex-M4 RISC integrated circuit. In this case, one controller is dedicated to controlling the laser in a highly reproducible manner required for maintaining tight temperature control with a commercial PI temperature controller package. In large part, the use of highly efficient microcontrollers resulted in a system that consumed only 2.0 W and could run for several hours on a pair of small, rechargeable batteries. The resulting total hardware cost of the instrument is mainly due to the laser, detector, and optics. The remaining components (Teensys, board, and various electronics) total ~$300.

A list of components with manufacturer, model, mass, power consumption, and price at the time of purchase, is shown in Table 1:

Component	Part #	Manufacturer	Mass (g)	Cost ($)	Power (W)
Electronics Box	PN-1324-C	Solutions Direct	417	25	n/a
Custom printed circuit board		OSH Park	36	65	-
Distributed Feedback Laser	NLK1E56AA	NTT Innovative Devices		1700	0.325
Temperature controller	WTC 3243	Wavelength Electronics		100	0.50
Microcontrollers	Teensy (3.6 or 4.1)	PJRC		60	0.80
Power conditioning	miscellaneous	miscellaneous		20	0.40
Batteries	ARB-L16-700UP	Fenix		20	**
Detector amplifier circuit	miscellaneous	miscellaneous		15	0.025
Collimating lens, card cage, mounts	CP33 x2, SR8 x4, CFC11A-C	Thorlabs	916	300	n/a
InGaAs detector	FD1500	Fermionics		200	n/a
Total			**1333**	**2500**	**2.05**

Since this project was undertaken, the Teensy family of microcontrollers has been impacted by global supply chain shortages of chips. Thus, the Teensy 3.6 is no longer available, and an alternative is needed to drive the laser. The primary

Deleted: boundary layer.
Deleted:
Deleted: .
Deleted: (COTS)
Deleted:
Deleted: Teensy's
Deleted: Mfc.
Deleted:
Deleted: misc
Deleted: misc
Deleted: misc
Deleted: misc
Deleted: was

consideration is that the laser driving function must be highly reproducible, both in ramp frequency and in power, to maintain precise tuning of the DFB output wavelength across the scan window. Replicating the measurements shown here would require generating ~1000 points per scan at a rate of 10 Hz (i.e., 10 ksps), with 12-bit resolution and uniform time steps for each update of the DAC. Several microcontrollers have demonstrated this level of performance, including the ItsyBitsy M4 Express, which also employs the Cortex-M4 processor and fast 12-bit true analog DAC. It would also be straightforward to use the Teensy 4.1 digital lines to drive a commercial DAC chip such as the AD5638 series from Analog Devices. Also noteworthy, we have carried out tests showing that full scans of ~1000 Hz are possible with the Teensy 3.6 and some of these alternatives, potentially enabling high-accuracy sampling at 10 to 100 times the rates shown here, albeit with reduced precision.

Throughout this work, we experimented with other designs, including the components that convert the voltage into current to drive the laser output, different configurations for the transimpedance amplifier, and lower voltage electronics that allow for the operation of a single 3.6 V lithium battery. In all cases, similar high performance was maintained. For example, we have successfully powered the laser with a miniature low-power diode laser driver (FL500, Wavelength Electronics, Bozeman, MT). The FL500 also offers additional useful features such as overvoltage protection and enable/disable pins to protect the laser. Out of convenience, all the results shown here were obtained with a simple transimpedance amplifier circuit with the op-amp powered by 5 V, and with zero bias on the InGaAs detector. It is possible to further reduce detector/amplifier noise by biasing the InGaAs detector with -2.5 V. Finally, we have successfully demonstrated that significantly lower power consumption is possible by using components that operate at 3.3 V, thus eliminating the need for two 3.6 V batteries in series.

One of the initial goals of this work was to develop a package that allows for quick swapping of lasers and optics in the field. This is achieved by using a DFB laser in a standard butterfly package integrated with TECs and a fiber-coupled FC/APC connector. Such an approach allows for swapping electronics with different lasers for probing different gases or for swapping optical systems allowing for different optical path lengths required to achieve adequate sensitivity, including options for employing folded optics such as Herriott cells or retroreflectors. Future applications envisioned by our laboratory include measurements of water vapor from stratospheric balloons, on small unattended aerial vehicles, and autonomous measurements from meteorological stations in remote locations, such as on buoys, the Antarctic plateau, or mountain peaks.

Deleted: some
Deleted: over the water
Deleted: -to100-
Deleted: the course of
Deleted: off
Deleted: tested
Deleted: with
Deleted: Cells
Deleted: including
Deleted: configuring for use

5 Conclusion

We have developed an economical and flexible fast-response TDLS suitable for measurements of water vapor in the ABL. The instrument bridges the current gap between research-grade instruments costing tens of thousands of dollars and low-cost sensors commonly employed in portable meteorological stations and hand-held devices. The novel feature of the new instrument is the use of a pair of low-cost, low-power microprocessors based on the Cortex-M4 ARM family of integrated circuits. A series of intercomparisons with existing instruments used for high-accuracy measurements of water vapor, including for eddy covariance, demonstrates that the new instrument is well suited for similar measurements for a fraction of the cost of existing instruments. Such a capability allows users with little previous expertise in instrumentation to acquire high-quality,

Deleted: tunable diode laser spectrometer
Deleted: atmospheric boundary layer (
Deleted:).
Deleted:
Deleted: TDLS
Deleted:
Deleted: TDLS
Deleted:

fast-response observations of water vapor for a variety of applications, including frequent horizontal and vertical profiling by uncrewed aerial vehicles, long-term eddy covariance measurements from fixed and portable flux towers, and routine measurements of humidity from weather stations in remote locations such as the polar ice caps, mountains, and glaciers.

Code availability: The extraction codes and Arduino sketches are available open source on GitHub.

Data availability: The data and circuit designs used in this paper are available from the corresponding author upon request.

Competing Interests: Some authors are members of the editorial board of the journal AMT.

Author Contributions: DT conceived and managed the project, including acquiring funding. The new TDLS was designed and fabricated by DT, EW, and LK. EW developed code for operating and extracting data from the TDLS. EW performed experimental work and data analysis, with assistance from DT. The drafting of the manuscript was coordinated by EW with contributions from all three authors.

Deleted: Drafting

Acknowledgments: We thank David Noone and Adriana Bailey for assistance with the operation and maintenance of the Picarro CRDS. We thank Scott Kittelman for access to the ATOC Skywatch Observatory and technical support for field measurements.

Deleted: for

Financial support: Seed funding for this project was provided by the University of Colorado. Some material is based upon work supported by the National Science Foundation under Grant No. AGS-2233136 and by the National Aeronautics and Space Administration Earth Sciences Division, Award No. 80NSSC20K0729. Any opinions, findings, conclusions or recommendations expressed in this material are those of the authors and do not necessarily reflect the views of the National Science Foundation, NASA, or the University of Colorado.

.

References

LI-7000 CO2/H2O instruction manual, LICOR Biosciences https://www.licor.com/env/pdf/gas_analyzers/7000/LI-7000Manual.pdf. 22 October 2023.

Aslan, T., Peltola, O., Ibrom, A., Nemitz, E., Rannik, Ü., and Mammarella, I.: The high-frequency response correction of eddy covariance fluxes – Part 2: An experimental approach for analysing noisy measurements of small fluxes, Atmos. Meas. Tech., 14, 5089–5106, https://doi.org/10.5194/amt-14-5089-2021, 2021.

Aubinet, M., Vesala, T., and Papale, D. (Eds.): Eddy Covariance: A Practical Guide to Measurement and Data Analysis, Springer Netherlands, Dordrecht, https://doi.org/10.1007/978-94-007-2351-1, 2012.

Bärfuss, K. B., Schmithüsen, H., and Lampert, A.: Drone-based meteorological observations up to the tropopause – a concept study, Atmos. Meas. Tech., 16, 3739–3765, https://doi.org/10.5194/amt-16-3739-2023, 2023.

Brotzge, J. A., Berchoff, D., Carlis, D. L., Carr, F. H., Carr, R. H., Gerth, J. J., Gross, B. D., Hamill, T. M., Haupt, S. E., Jacobs, N., McGovern, A., Stensrud, D. J., Szatkowski, G., Szunyogh, I., and Wang, X.: Challenges and Opportunities in Numerical Weather Prediction, Bulletin of the American Meteorological Society, 104, E698–E705, https://doi.org/10.1175/BAMS-D-22-0172.1, 2023.

Burns, S. P., Delany, A. C., Sun, J., Stephens, B. B., Oncley, S. P., Maclean, G. D., Semmer, S. R., Schröter, J., and Ruppert, J.: An Evaluation of Calibration Techniques for In Situ Carbon Dioxide Measurements Using a Programmable Portable Trace-Gas Measuring System, Journal of Atmospheric and Oceanic Technology, 26, 291–316, https://doi.org/10.1175/2008JTECHA1080.1, 2009.

Couvreux, F., Guichard, F., Austin, P. H., and Chen, F.: Nature of the Mesoscale Boundary Layer Height and Water Vapor Variability Observed 14 June 2002 during the IHOP_2002 Campaign, Monthly Weather Review, 137, 414–432, https://doi.org/10.1175/2008MWR2367.1, 2009.

Davis, S. M., Hallar, A. G., Avallone, L. M., and Engblom, W.: Measurement of Total Water with a Tunable Diode Laser Hygrometer: Inlet Analysis, Calibration Procedure, and Ice Water Content Determination, Journal of Atmospheric and Oceanic Technology, 24, 463–475, https://doi.org/10.1175/JTECH1975.1, 2007.

Dorsi, S. W., Kalnajs, L. E., Toohey, D. W., and Avallone, L. M.: A fiber-coupled laser hygrometer for airborne total water measurement, Atmos. Meas. Tech., 7, 215–223, https://doi.org/10.5194/amt-7-215-2014, 2014.

Fabry, F.: The Spatial Variability of Moisture in the Boundary Layer and Its Effect on Convection Initiation: Project-Long Characterization, Monthly Weather Review, 134, 79–91, https://doi.org/10.1175/MWR3055.1, 2006.

Fischer, L., Kiemle, C., and Craig, G. C.: Height-resolved variability of midlatitude tropospheric water vapor measured by an airborne lidar: MOISTURE VARIABILITY FROM AIRBORNE LIDAR, Geophys. Res. Lett., 39, n/a-n/a, https://doi.org/10.1029/2011GL050621, 2012.

Geerts, B., Raymond, D. J., Grubišić, V., Davis, C. A., Barth, M. C., Detwiler, A., Klein, P. M., Lee, W.-C., Markowski, P. M., Mullendore, G. L., and Moore, J. A.: Recommendations for In Situ and Remote Sensing Capabilities in Atmospheric Convection and Turbulence, Bulletin of the American Meteorological Society, 99, 2463–2470, https://doi.org/10.1175/BAMS-D-17-0310.1, 2018.

Gordon, I. E., Rothman, L. S., Hargreaves, R. J., Hashemi, R., Karlovets, E. V., Skinner, F. M., Conway, E. K., Hill, C., Kochanov, R. V., Tan, Y., Wcisło, P., Finenko, A. A., Nelson, K., Bernath, P. F., Birk, M., Boudon, V., Campargue, A., Chance, K. V., Coustenis, A., Drouin, B. J., Flaud, J. –M., Gamache, R. R., Hodges, J. T., Jacquemart, D., Mlawer, E. J., Nikitin, A. V., Perevalov, V. I., Rotger, M., Tennyson, J., Toon, G. C., Tran, H., Tyuterev, V. G., Adkins, E. M., Baker, A., Barbe, A., Canè, E., Császár, A. G., Dudaryonok, A., Egorov, O., Fleisher, A. J., Fleurbaey, H., Foltynowicz, A., Furtenbacher, T., Harrison, J. J., Hartmann, J. –M., Horneman, V. –M., Huang, X., Karman, T., Karns, J., Kassi, S., Kleiner, I., Kofman, V., Kwabia–Tchana, F., Lavrentieva, N. N., Lee, T. J., Long, D. A., Lukashevskaya, A. A., Lyulin, O. M., Makhnev, V. Yu., Matt, W., Massie, S. T., Melosso, M., Mikhailenko, S. N., Mondelain, D., Müller, H. S. P., Naumenko, O. V., Perrin, A., Polyansky, O. L., Raddaoui, E., Raston, P. L., Reed, Z. D., Rey, M., Richard, C., Tóbiás, R., Sadiek, I., Schwenke, D. W., Starikova, E., Sung, K., Tamassia, F., Tashkun, S. A., Vander Auwera, J., Vasilenko, I. A., Vigasin, A. A., Villanueva, G. L., Vispoel, B., Wagner, G., Yachmenev, A., and Yurchenko, S. N.: The HITRAN2020 molecular spectroscopic database, Journal of Quantitative Spectroscopy and Radiative Transfer, 277, 107949, https://doi.org/10.1016/j.jqsrt.2021.107949, 2022.

Hallar, A. G., Avallone, L. M., Herman, R. L., Anderson, B. E., and Heymsfield, A. J.: Measurements of ice water content in tropopause region Arctic cirrus during the SAGE III Ozone Loss and Validation Experiment (SOLVE), J. Geophys. Res., 109, 2003JD004348, https://doi.org/10.1029/2003JD004348, 2004.

Helbig, M., Gerken, T., Beamesderfer, E. R., Baldocchi, D. D., Banerjee, T., Biraud, S. C., Brown, W. O. J., Brunsell, N. A., Burakowski, E. A., Burns, S. P., Butterworth, B. J., Chan, W. S., Davis, K. J., Desai, A. R., Fuentes, J. D., Hollinger, D. Y., Kljun, N., Mauder, M., Novick, K. A., Perkins, J. M., Rahn, D. A., Rey-Sanchez, C., Santanello, J. A., Scott, R. L., Seyednasrollah, B., Stoy, P. C., Sullivan, R. C., De Arellano, J. V.-G., Wharton, S., Yi, C., and Richardson, A. D.: Integrating continuous atmospheric boundary layer and tower-based flux measurements to advance understanding of land-atmosphere interactions, Agricultural and Forest Meteorology, 307, 108509, https://doi.org/10.1016/j.agrformet.2021.108509, 2021.

Henze, D., Noone, D., and Toohey, D.: Detection of dilution due to turbulent mixing vs. precipitation scavenging effects on biomass burning aerosol concentrations using stable water isotope ratios during ORACLES, Atmos. Chem. Phys., 23, 15269–15288, https://doi.org/10.5194/acp-23-15269-2023, 2023.

Kämpfer, N. (Ed.): Monitoring Atmospheric Water Vapour: Ground-Based Remote Sensing and In-situ Methods, Springer New York, New York, NY, https://doi.org/10.1007/978-1-4614-3909-7, 2013.

Kiemle, C., Wirth, M., Fix, A., Rahm, S., Corsmeier, U., and Di Girolamo, P.: Latent heat flux measurements over complex terrain by airborne water vapour and wind lidars, Quart J Royal Meteoro Soc, 137, 190–203, https://doi.org/10.1002/qj.757, 2011.

Kim, D.-G., Bond-Lamberty, B., Ryu, Y., Seo, B., and Papale, D.: Ideas and perspectives: Enhancing research and monitoring of carbon pools and land-to-atmosphere greenhouse gases exchange in developing countries, Biogeosciences, 19, 1435–1450, https://doi.org/10.5194/bg-19-1435-2022, 2022.

Markwitz, C. and Siebicke, L.: Low-cost eddy covariance: a case study of evapotranspiration over agroforestry in Germany, Atmos. Meas. Tech., 12, 4677–4696, https://doi.org/10.5194/amt-12-4677-2019, 2019.

May, R. D.: Open-path, near-infrared tunable diode laser spectrometer for atmospheric measurements of H_2O, J. Geophys. Res., 103, 19161–19172, https://doi.org/10.1029/98JD01678, 1998.

May, R. D. and Webster, C. R.: Data processing and calibration for tunable diode laser harmonic absorption spectrometers, Journal of Quantitative Spectroscopy and Radiative Transfer, 49, 335–347, https://doi.org/10.1016/0022-4073(93)90098-3, 1993.

Miloshevich, L. M., Paukkunen, A., Vömel, H., and Oltmans, S. J.: Development and Validation of a Time-Lag Correction for Vaisala Radiosonde Humidity Measurements, J. Atmos. Oceanic Technol., 21, 1305–1327, https://doi.org/10.1175/1520-0426(2004)021<1305:DAVOAT>2.0.CO;2, 2004.

Miloshevich, L. M., Vömel, H., Whiteman, D. N., and Leblanc, T.: Accuracy assessment and correction of Vaisala RS92 radiosonde water vapor measurements, J. Geophys. Res., 114, D11305, https://doi.org/10.1029/2008JD011565, 2009.

Muller, C. L., Chapman, L., Johnston, S., Kidd, C., Illingworth, S., Foody, G., Overeem, A., and Leigh, R. R.: Crowdsourcing for climate and atmospheric sciences: current status and future potential, Intl Journal of Climatology, 35, 3185–3203, https://doi.org/10.1002/joc.4210, 2015.

Newell, R. E., Zhu, Y., Browell, E. V., Ismail, S., Read, W. G., Waters, J. W., Kelly, K. K., and Liu, S. C.: Upper tropospheric water vapor and cirrus: Comparison of DC-8 observations, preliminary UARS microwave limb sounder measurements and meteorological analyses, J. Geophys. Res., 101, 1931–1941, https://doi.org/10.1029/95JD01373, 1996.

Noone, D., Galewsky, J., Sharp, Z. D., Worden, J., Barnes, J., Baer, D., Bailey, A., Brown, D. P., Christensen, L., Crosson, E., Dong, F., Hurley, J. V., Johnson, L. R., Strong, M., Toohey, D., Van Pelt, A., and Wright, J. S.: Properties of air mass mixing and humidity in the subtropics from measurements of the D/H isotope ratio of water vapor at the Mauna Loa Observatory: WATER AND ISOTOPE MIXING AT MAUNA LOA, J. Geophys. Res., 116, n/a-n/a, https://doi.org/10.1029/2011JD015773, 2011.

Ocheltree, T. W. and Loescher, H. W.: Design of the AmeriFlux Portable Eddy Covariance System and Uncertainty Analysis of Carbon Measurements, Journal of Atmospheric and Oceanic Technology, 24, 1389–1406, https://doi.org/10.1175/JTECH2064.1, 2007.

Ogunjemiyo, S., Roberts, D. A., Keightley, K., Ustin, S. L., Hinckley, T., and Lamb, B.: Evaluating the relationship between AVIRIS water vapor and poplar plantation evapotranspiration, J.-Geophys.-Res., 107, https://doi.org/10.1029/2001JD001194, 2002.

Petersen, R. A.: On the Impact and Benefits of AMDAR Observations in Operational Forecasting—Part I: A Review of the Impact of Automated Aircraft Wind and Temperature Reports, Bulletin of the American Meteorological Society, 97, 585–602, https://doi.org/10.1175/BAMS-D-14-00055.1, 2016.

Pillar-Little, E. A., Greene, B. R., Lappin, F. M., Bell, T. M., Segales, A. R., De Azevedo, G. B. H., Doyle, W., Kanneganti, S. T., Tripp, D. D., and Chilson, P. B.: Observations of the thermodynamic and kinematic state of the atmospheric boundary layer over the San Luis Valley, CO, using the CopterSonde 2 remotely piloted aircraft system in support of the LAPSE-RATE field campaign, Earth Syst. Sci. Data, 13, 269–280, https://doi.org/10.5194/essd-13-269-2021, 2021.

Pokorný, R., Slípková, R., Havránková, K., and Pavelka, M.: ECOSYSTEM WATER USE EFFICIENCY OF NORWAY SPRUCE MONOCULTURE FROM EDDY-COVARIANCE AND ECOPHYSIOLOGICAL MEASUREMENTS, Acta Hortic., 301–307, https://doi.org/10.17660/ActaHortic.2012.951.36, 2012.

Rainwater, B. J.: A New Approach for Ratiometric Measurements of Water Isotopologues, University of Colorado Boulder, 2022.

Roth, H. A. and Blanken, P. D.: Controls and rates of evaporation from a water supply reservoir in the Colorado Front Range, Journal of Hydrology, 617, 129139, https://doi.org/10.1016/j.jhydrol.2023.129139, 2023.

Santanello, J. A., Dirmeyer, P. A., Ferguson, C. R., Findell, K. L., Tawfik, A. B., Berg, A., Ek, M., Gentine, P., Guillod, B. P., Van Heerwaarden, C., Roundy, J., and Wulfmeyer, V.: Land–Atmosphere Interactions: The LoCo Perspective, Bulletin of the American Meteorological Society, 99, 1253–1272, https://doi.org/10.1175/BAMS-D-17-0001.1, 2018.

Segales, A. R., Greene, B. R., Bell, T. M., Doyle, W., Martin, J. J., Pillar-Little, E. A., and Chilson, P. B.: The CopterSonde: an insight into the development of a smart unmanned aircraft system for atmospheric boundary layer research, Atmos. Meas. Tech., 13, 2833–2848, https://doi.org/10.5194/amt-13-2833-2020, 2020.

Segales, A. R., Chilson, P. B., and Salazar-Cerreño, J. L.: Considerations for improving data quality of thermo-hygrometer sensors on board unmanned aerial systems for planetary boundary layer research, Atmos. Meas. Tech., 15, 2607–2621, https://doi.org/10.5194/amt-15-2607-2022, 2022.

Shivers, S. W., Roberts, D. A., McFadden, J. P., and Tague, C.: An analysis of atmospheric water vapor variations over a complex agricultural region using airborne imaging spectrometry, PLoS ONE, 14, e0226014, https://doi.org/10.1371/journal.pone.0226014, 2019.

Trenberth, K. E., Fasullo, J., and Smith, L.: Trends and variability in column-integrated atmospheric water vapor, Climate Dynamics, 24, 741–758, https://doi.org/10.1007/s00382-005-0017-4, 2005.

Trent, T., Boesch, H., Somkuti, P., and Scott, N.: Observing Water Vapour in the Planetary Boundary Layer from the Short-Wave Infrared, Remote Sensing, 10, 1469, https://doi.org/10.3390/rs10091469, 2018.

Varentsov, M., Konstantinov, P., Repina, I., Artamonov, A., Pechkin, A., Soromotin, A., Esau, I., and Baklanov, A.: Observations of the urban boundary layer in a cold climate city, Urban Climate, 47, 101351, https://doi.org/10.1016/j.uclim.2022.101351, 2023.

Werle, P., M□cke, R., and Slemr, F.: The limits of signal averaging in atmospheric trace-gas monitoring by tunable diode-laser absorption spectroscopy (TDLAS), Appl. Phys. B, 57, 131–139, https://doi.org/10.1007/BF00425997, 1993.

Wu, J. B., Zhou, X. Y., Wang, A. Z., and Yuan, F. H.: Comparative measurements of water vapor fluxes over a tall forest using open- and closed-path eddy covariance system, Atmos. Meas. Tech., 8, 4123–4131, https://doi.org/10.5194/amt-8-4123-2015, 2015.

Wulfmeyer, V., Hardesty, R. M., Turner, D. D., Behrendt, A., Cadeddu, M. P., Di Girolamo, P., Schlüssel, P., Van Baelen, J., and Zus, F.: A review of the remote sensing of lower tropospheric thermodynamic profiles and its indispensable role for the understanding and the simulation of water and energy cycles, Reviews of Geophysics, 53, 819–895, https://doi.org/10.1002/2014RG000476, 2015.

Zhao, C. L. and Tans, P. P.: Estimating uncertainty of the WMO mole fraction scale for carbon dioxide in air, J. Geophys. Res., 111, 2005JD006003, https://doi.org/10.1029/2005JD006003, 2006.